NUCLEAR SCIENCE AND ENGINEERING: **132**, 1–15 (1999)

Neutron Yields from 155 MeV/Nucleon Carbon and Helium Stopping in Aluminum

L. Heilbronn*

Lawrence Berkeley National Laboratory, MS 29-100, Berkeley, California 94720

R. S. Cary†

Virginia State University, Department of Physics, Petersburg, Virginia 23806

M. Cronqvist

Lawrence Berkeley National Laboratory, MS 50-245, Berkeley, California 94720

F. Deák

Eötvös University, Department of Atomic Physics, Budapest 114, Hungary H-1088

K. Frankel

Lawrence Berkeley National Laboratory, MS 84-171, Berkeley, California 94720

A. Galonsky

Michigan State University, National Superconducting Cyclotron Laboratory and Department of Physics East Lansing, Michigan 48824

K. Holabird‡

San Francisco State University, Department of Physics, San Francisco, California 94132

Á. Horvath and Á. Kiss

Eötvös University, Department of Atomic Physics, Budapest 114, Hungary H-1088

J. Kruse and R. M. Ronningen

Michigan State University, National Superconducting Cyclotron Laboratory and Department of Physics East Lansing, Michigan 48824

H. Schelin

CEFET-PR Department of Physics, 80230-901 Curitiba-PR, Brazil

Z. Seres

KFKI Research Institute for Particle and Nuclear Physics, Budapest 114, Hungary H-1525

*E-mail: LHHeilbronn@LBL.gov

†Current address: Naval Surface Warfare Center, Dahlgren, Virginia 22448.

‡Current address: Spectra-Physics Lasers, 1335 Terra Bella Avenue, Building 15, Mountain View, California 94043.

C. E. Stronach

Virginia State University, Department of Physics, Petersburg, Virginia 23806

J. Wang and P. Zecher§

Michigan State University, National Superconducting Cyclotron Laboratory and Department of Physics East Lansing, Michigan 48824

and

C. Zeitlin

Lawrence Berkeley National Laboratory, MS 29-100, Berkeley, California 94720

Received March 31, 1998
Accepted September 17, 1998

Abstract – *Neutron fluences have been measured from 155 MeV/nucleon ^{4}He and ^{12}C ions stopping in an Al target at laboratory angles between 10 and 160 deg. The resultant spectra were integrated over angle and energy above 10 MeV to produce total neutron yields. Comparison of the two systems shows that approximately two times as many neutrons are produced from 155 MeV/nucleon ^{4}He stopping in Al and 155 MeV/nucleon ^{12}C stopping in Al. Using an energy-dependent geometric cross-section formula to calculate the expected number of primary nuclear interactions shows that the ^{12}C + Al system has, within uncertainties, the same number of neutrons per interaction (0.99 ± 0.03) as does the ^{4}He + Al system (1.02 ± 0.04), despite the fact that ^{12}C has three times as many neutrons as does ^{4}He. Energy and angular distributions for both systems are also reported. No major differences can be seen between the two systems in those distributions, except for the overall magnitude. Where possible, the ^{4}He + Al spectra are compared with previously measured spectra from 160 and 177.5 MeV/nucleon ^{4}He interactions in a variety of stopping targets. The reported spectra are consistent with previously measured spectra. The data were acquired to provide data applicable to problems dealing with the determination of the radiation risk to humans engaged in long-term missions in space; however, the data are also of interest for issues related to the determination of the radiation environment in high-altitude flight, with shielding at high-energy heavy-ion accelerators and with doses delivered outside tumor sites treated with high-energy hadronic beams.*

I. INTRODUCTION

To estimate the risk to humans exposed to a radiation field in a shielded environment, it is not enough to know only the details of the primary radiation field. The nature of the primary radiation field is significantly altered as it is transported through the shielding, creating a secondary radiation field behind the shielding that must also be characterized. In some scenarios, the dose and dose equivalent received from neutrons present in the secondary radiation field constitute a significant fraction of the total dose and dose equivalent. For example, cone calculation predicts that ~50% of the dose equivalent on a Martian or lunar base made up of 50 g/cm^2 of regolith comes from neutrons.[1] Similarly, initial studies and measurements done for the National Aeronautics and Space Administration's (NASA's) proposed high-speed civil transport indicate that neutrons make a major contribution to the dose rate at high altitudes.[2] Secondary neutrons are also an important component of the dose equivalent behind shielding at accelerator facilities and in areas of the human body near tumor sites that are treated with high-energy hadronic beams.

In a thickly shielded lunar or Martian base, or in the upper atmosphere, neutrons are generated by interactions of primary galactic cosmic rays (GCRs) and solar radiation with shielding materials such as regolith or the atmosphere. The GCRs consist of 98% hadrons, of which 87% are protons, 12% are He, and 1% are heavier ions.[3] Most of the GCR fluence has kinetic energies between 100 MeV/nucleon and 10 GeV/nucleon, with the maximum fluence occurring between 300 and 600 MeV/nucleon, independent of particle mass. Because neutrons are produced in interactions that span a large range in projectile mass and energy, as well as target (shielding) mass, calculational methods are the best approach to estimating the dose from neutrons in such scenarios. However, those calculational methods (Refs. 1, 4, and 5, for example) still require an extensive set of neutron production cross sections for input into the codes and thick-target neutron yields for verification of the codes' output. The data sets needed for those codes should be large

§Deloitte and Touche, New York, New York.

enough to establish the dependency of neutron production on the projectile's mass and energy and on the target's mass.

Although particles heavier than He make up just 1% of the GCR, a calculation has shown that ~16% of the neutron flux behind 50 g/cm^2 of water comes from the fragmentation of those particles (15% of the flux comes from interactions with GCR He nuclei, with the remainder from proton-induced interactions).[5] Calculations such as those done in Refs. 1, 4, and 5 make several assumptions regarding neutron production from heavy-ion interactions because of the relative lack of pertinent experimental data. For example, in Ref. 6 the neutron production from heavy ions is generated from a simple scaling using measured proton-induced neutron cross sections and yields. Scaling heavy-ion neutron yields from proton-induced reactions will miss the component of the yield due to the breakup of the projectile, which is significant at forward angles.

In atmospheric neutrons, only 25 to 30% of the predicted dose equivalent comes from the measured fast neutron (1- to 10-MeV) component; the remaining 70% comes from unverified theoretical predictions of the neutron yield above 10 MeV. Furthermore, it is believed that current atmospheric environmental models may be significantly underpredicting the yield of high-energy (>10-MeV) neutrons.[2,7]

The neutron yields from 155 MeV/nucleon ^{12}C and ^{4}He stopping in an Al target have been measured to provide some information on the nature of the high-energy neutron yield as well as to investigate the dependence of the neutron yield on projectile mass. Neutron yields were measured at laboratory angles between 10 and 160 deg and for neutron energies of 10 MeV and above. In addition to the neutron spectra at each angle, we present angular distributions and energy distributions from each system as well as total neutron yields.

II. EXPERIMENTAL DETAILS

The data presented in this paper come from a neutron time-of-flight (TOF) experiment that was performed at Michigan State University's National Superconducting Cyclotron Laboratory (NSCL). Beams of fully stripped 155 MeV/nucleon ^{12}C and ^{4}He were delivered on target in 1- to 3-ns-wide bursts. In each case the period of the beam burst was 41.6 ns. Beam spot size at the target was typically 0.5 cm in diameter. For normalization purposes, the number of beam particles incident on the target was calculated from the total amount of charge collected in the Al target as read by a current integrator. The target was a 13.34-cm-long, 1.78-cm-diam cylinder of Al with a 5.08-cm-long, 1.59-cm-diam bore cut into the entrance of the target (the beam's axis coincided with the target's cylindrical axis). The target bore minimized the loss of backscattered delta electrons, which improved the charge-collection properties of the target. The target was suspended inside a 91.44-cm-diam steel scattering chamber with 3.2-mm-thick walls. Typical pressure inside the scattering chamber and beam line was 10^{-6} Torr.

Neutron detectors were placed outside the scattering chamber at laboratory angles between 10 and 160 deg. Each neutron detector consisted of a liquid scintillator (BC-501 or NE-213) encased in a cylindrical cell constructed of either glass or Al. The detector cells were typically 12.7 cm in diameter and either 7.62 or 5.08 cm long. Arrays of seven neutron detectors bundled together were placed at 10, 30, 45, and 60 deg. An array of three detectors was placed at 90 deg, and individual detectors were placed at 125, 160, −30, −45, and −60 deg (a minus sign indicates the detectors were placed on the right side of the beam). Solid plastic scintillators 6.35 mm thick and 12.7 cm in diameter, referred to as *veto detectors*, were placed between the neutron detectors and the target to register any events in the neutron detectors created by charged particles energetic enough to traverse the materials lying between the target and the neutron detector. Cylindrical bars of brass or steel were periodically placed between the target and the neutron detectors to stop neutrons coming directly from the target. These allowed only background neutrons, such as room-scattered neutrons, to hit the neutron detectors. Figure 1 shows an overhead view of the experimental setup. Tables I, II, and III contain information regarding the neutron detectors, veto detectors, and shadow bars.

Data were recorded on an event-by-event basis. A master trigger was generated by any event in a neutron detector that was above the detector's constant fraction discriminator's (CFD's) threshold. The CFD thresholds were typically set to one to three times the ^{60}Co Compton edge. For each event the following information was recorded:

1. number of the neutron detector in which the event took place
2. total charge collected in the anode pulse from the neutron detector
3. charge collected in the tail of the anode pulse from the detector
4. relative time between the event in the neutron detector and a radio-frequency (rf) signal from the cyclotron
5. flag indicating whether or not the companion veto detector also registered an event
6. total amount of charge collected in the anode signal from the veto detector.

In addition, information regarding the live time, total charge collected in the target, total number of events in each detector, and prescale factors was recorded from each run.

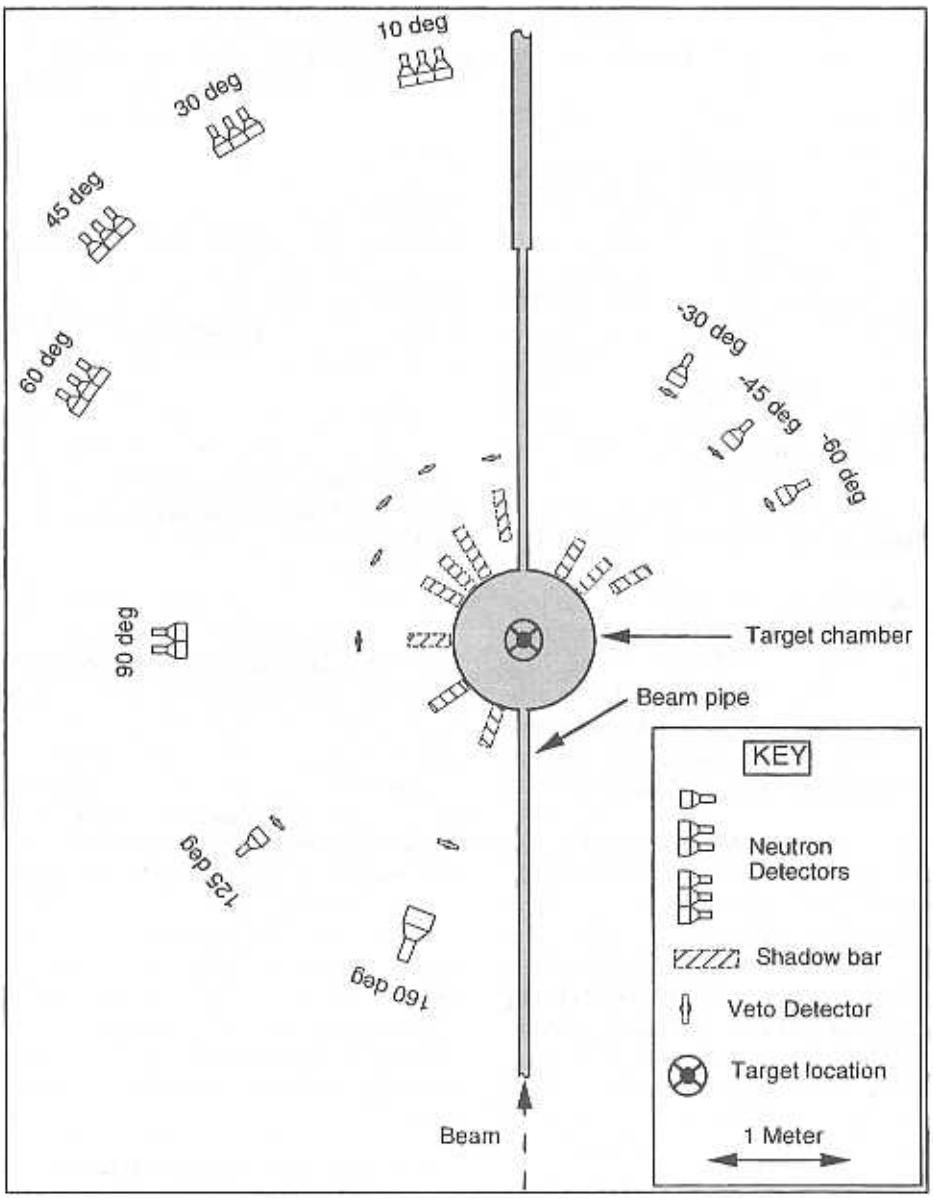

Fig. 1. Overhead view of the experimental setup in the N4 vault at the NSCL.

III. DATA ANALYSIS

III.A. Neutron Energy Determination

Neutron energies were determined by measuring the TOF between a signal from cyclotron rf and a timing signal generated from the anode of the neutron detector. The rf signals were prescaled by a factor of 4 so that groups of four sequential beam bursts were timed against a single rf signal. Prescaling the rf signal by a factor of 4 ensures that the maximum time difference between an rf signal and a signal from the neutron detector is at least three times the rf period (3×41.6 ns), which enables us to measure neutrons energies down to the desired goal of 10 MeV. Figure 2 shows the time-to-digital converter (TDC) spectrum for neutron detector 33 (160 deg). Time increases from right to left. Gamma-ray events are shown with the solid histogram, and neutron events are shown with the dotted histogram. The peaks labeled A, B, C, and D are from prompt gamma rays created by separate beam bursts striking the target. The widths (full-width at half-maximum) of those peaks have an average value of ~1 ns, and that value is used as the overall timing resolution in the experiment, which in turn is used to set the minimum bin width in the energy spectra generated from the TDC spectra. Neutron events were separated off-line

TABLE I

Position, Flight Path, and Solid Angle Subtended by the Neutron Detectors Used in the Experiment*

Detector Number	Angle (deg)	Flight Path (cm)	Solid Angle (msr)
1	10	404.1	0.775 (2.6, 3.7)
2	10	405.3	0.720 (2.5, 3.7)
3	10	404.9	0.697 (2.6, 3.7)
4	10	404.9	0.773 (2.6, 3.8)
5	10	404.9	0.773 (2.6, 3.8)
6	10	406.2	0.768 (2.0, 3.1)
7	10	405.2	0.772 (2.6, 3.8)
8	30	404.1	0.776 (2.4, 3.6)
9	30	405.9	0.769 (1.8, 2.9)
10	30	405.9	0.741 (2.3, 3.4)
11	30	405.2	0.732 (2.5, 3.6)
12	30	406.2	0.768 (1.8, 2.9)
13	30	405.1	0.726 (2.3, 3.4)
14	30	405.9	0.741 (2.3, 3.4)
15	45	403.8	0.787 (2.3, 3.2)
16	45	406.2	0.768 (1.7, 2.6)
17	45	404.9	0.773 (2.3, 3.2)
18	45	405.1	0.729 (2.3, 3.2)
19	45	404.9	0.773 (2.3, 3.2)
20	45	405.1	0.732 (2.3, 3.2)
21	45	405.0	0.733 (2.2, 3.2)
22	60	353.8	1.025 (2.4, 3.1)
23	60	354.3	0.772 (1.9, 2.7)
24	60	354.1	1.023 (2.4, 3.1)
25	60	354.1	1.023 (2.4, 3.1)
26	60	354.1	1.023 (2.4, 3.1)
27	60	354.1	1.023 (2.4, 3.1)
28	60	354.1	1.023 (2.4, 3.1)
29	90	243.1	2.144 (2.1, 2.1)
30	90	242.1	2.040 (3.1, 3.1)
31	90	241.8	1.955 (3.2, 3.2)
32	125	232.9	2.335 (3.9, 5.1)
33	160	202.6	7.901 (5.0, 7.4)
35	−30	203.8	3.088 (4.7, 6.9)
36	−45	204.9	2.849 (4.6, 6.4)
37	−60	204.9	3.017 (4.3, 5.6)

*The flight paths are measured from the target to the center of the detector. The two numbers in parentheses are the percent of systematic uncertainties in the solid angle for the ^{12}C run and the ^{4}He run, respectively (see text).

TABLE II

Position and Flight Path for the Veto Detectors Used in the Experiment*

Veto Detector Angle (deg)	Flight Path (cm)
10	116.8
30	125.7
45	125.1
60	100.3
90	106.0
125	221.0
160	154.8
−30	194.3
−45	190.5
−60	193.0

*The flight paths are measured from the target to the center of the detector.

TABLE III

Position, Length, Diameter, and Flight Path for the Shadow Bars Used in the Experiment*

Angle (deg)	Length (cm)	Diameter (cm)	Flight Path (cm)
10	36.8	10.16	81.9
30	40.6	8.89	66.0
45	29.8	8.89	60.6
60	30.2	10.16	60.8
90	30.5	10.16	61.0
125	29.5	7.62	60.5
160	29.5	7.62	60.5
−30	29.5	7.62	60.3
−45	29.5	7.62	60.5
−60	29.5	7.62	78.9

*The flight paths are measured from the target to the center of the shadow bar.

from gamma-ray events using the technique described by Heltsley et al.,[8] which takes advantage of the different pulse shapes created by neutron- and gamma-ray-induced events in the liquid-scintillator cell. By plotting the amount of charge in the tail of the pulse as a function of the amount of charge in the entire pulse, two distinct lines, one each for neutron and for gamma-ray events, could be seen and used to separate the two classes of events.

The TDC spectra were calibrated by measuring the number of channels between prompt gamma-ray peaks and using the known period (41.6 ns) of the beam bursts. The TOF for a neutron event is calculated using the measured difference between it and the nearest prior prompt gamma-ray peak and adding to that the TOF for a gamma ray to go from the target to the neutron detector. For example, a neutron event in channel n of Fig. 2 has the corresponding TOF:

$$\mathrm{TOF}_n = [k(\mathrm{CHAN}_C - \mathrm{CHAN}_n)] + \mathrm{TOF}_g \ , \qquad (1)$$

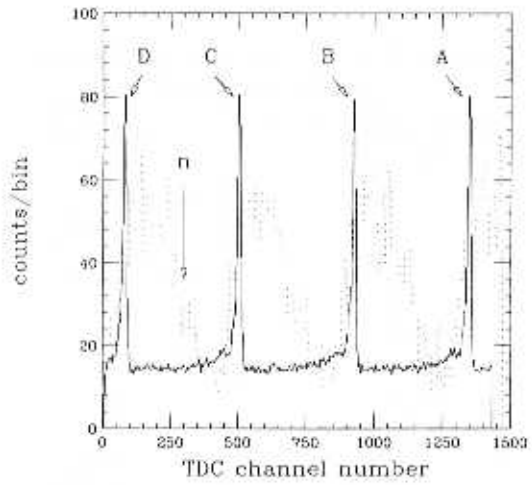

Fig. 2. The TDC spectrum for detector 33. Time increases from right to left. Gamma-ray events are indicated with the solid histogram, and neutron events are indicated with the dotted histogram. The peaks labeled A, B, C, and D are due to prompt gamma rays created by successive beam bursts striking the target.

where

$CHAN_c$ = TDC channel number of the prompt gamma-ray peak labeled C in Fig. 2

$CHAN_n$ = TDC channel number of n

k = TDC channel-to-time conversion factor

TOF_n = TOF for a prompt gamma ray to go from the target to the neutron detector.

Using the flight path from target to detector, the neutron's velocity is calculated from its TOF. The neutron's energy is then calculated from its velocity using relativistic kinematics.

III.B. Background Subtraction

In addition to the neutrons that go directly from the target to the neutron detector, the neutron detectors also register background events resulting from room-scattered neutrons that go indirectly from the target into the detector. Shadow bars (see Sec. II) were placed between the target and the neutron detectors at various times during the experiment, which allowed the measurement of only the background neutrons. Runs without the shadow bars measured both the direct and the background neutrons. By subtracting the shadow-bar raw data from the non-shadow-bar raw data (after normalizing the runs to each other for run time, computer live time, etc.), the direct neutron spectra were separated from the background spectra.

III.C. Wraparound Neutrons and (Q) Charge-to-Digital Converter Calibration

III.C.1. Low-Energy Wraparound Neutrons

As can be seen in Fig. 2, an event in the TDC spectrum may come from any one burst in a set of sequential beam bursts. For example, an event that occurs in the channel labeled n in Fig. 2 may be a relatively high energy neutron that came from the beam burst that produced the prompt gamma-ray peak C, or it may be a much lower energy neutron that came from the beam burst corresponding to peak B. Such a low-energy neutron from a preceding beam burst is referred to as a wraparound neutron. Equation (1) is not valid for wraparound neutrons, and those neutrons must be removed from the raw data before energy spectra are produced.

The first step in eliminating low-energy wraparound neutrons is to determine the energy at which neutrons from a preceding beam burst start to wrap around with neutrons from the beam burst that is used in Eq. (1). That value was found by computing the energy of a neutron (referred to as the wraparound energy) from the preceding burst that occurs in the prompts-gamma peak location of the beam burst used in Eq. (1). For example, in Fig. 2, the energy of a neutron coming from beam burst B that has the same TDC value as the prompt-gamma-ray peak labeled C is 9.3 MeV. Thus, all neutrons from beam burst B with energies 9.3 MeV and lower will wrap around with neutrons coming from beam burst C.

The next step is to apply a cut to the data that eliminates all neutrons with energies up to and including the low-energy wraparound energy. Although there is no direct measure of the neutron's energy, the (Q) charge-to-digital converter (QDC) measures the amount of charge produced by light that is created in the scintillator via neutron interactions with charged particles in the liquid. A neutron of a given energy can produce any amount of light up to a maximum that is produced when the neutron has a direct collision with a proton, transferring all of its momentum to the proton. By making a cut on QDC values that corresponds to the maximum amount of light produced by a neutron with the wraparound energy, all wraparound neutrons can be eliminated, leaving only neutrons with energies greater than the wraparound energy. To continue the example in Fig. 2, finding the QDC value that corresponds to the light produced by a 9.3-MeV proton, and by eliminating all events that have that QDC value or lower, wraparound neutrons are eliminated from the data.

III.C.2. The (Q) Charge-to-Digital Converter Calibration

To correctly apply a QDC threshold to the data, the QDC spectra were converted to units of recoil-proton energy (equivalent to neutron energy for direct collisions).

Two different methods were used to convert QDC values to recoil-proton energy. The first method takes advantage of the fact that some protons created in the target have sufficient energy to reach the detector. Such events will have a positive veto signal. A scatter plot of QDC value compared with TDC value for these events shows a line that corresponds to high-energy protons. In some cases, lines corresponding to deuterons and tritons can also be observed. By choosing points along the proton line, one can determine the direct correspondence between QDC value and TOF of the proton. Furthermore, by knowing the thicknesses and the positions of materials that the proton went through to get to the neutron detector and by using proton-energy-loss tables,[9] the energy of a proton as it enters the neutron detectors can be calculated as a function of its TOF. Thus, a direct relationship between proton energy and QDC response is determined. A plot of QDC value as a function of proton energy for detector 9 (30 deg) is shown in Fig. 3. The values obtained using this method are indicated by the diamond-shaped symbols. At 30 deg the wraparound energy is 29.5 MeV, and the corresponding QDC threshold value then used to eliminate wraparound neutrons can be directly read from that plot.

The second method used to calibrate the QDC spectra involved producing a plot of the detector's QDC value as a function of TDC value but gated only on neutron events. In such plots a clear demarcation is observed between QDC values where a neutron can produce light via recoil and QDC values where it is kinematically impossible for a neutron of a given energy to produce such a value. The point of demarcation at a particular TDC value corresponds to the maximum amount of light produced by a neutron of the appropriate energy. The QDC value at the demarcation point is assumed to be equivalent to the amount of light produced by a proton that received the maximum amount of momentum transfer from the incoming neutron. Thus, by determining the neutron's energy from its TDC value and by assuming that the QDC value at the demarcation point is produced by a proton of the same energy, a second, independent set of values of QDC as a function of proton energy is generated. The values obtained using this method for detector 9 are indicated in Fig. 3 by the X-shaped symbols.

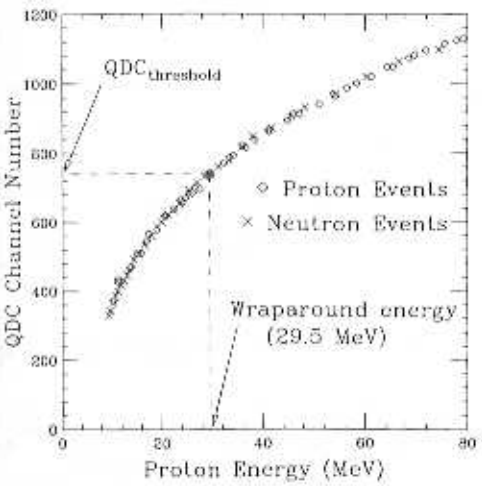

Fig. 3. Plot of QDC channel number as a function of recoil proton energy for detector 9. The two symbols represent two different methods used for obtaining the recoil proton energy, as described in the text.

The agreement between the two methods is good, in general. The two methods agreed with each other to no worse than ±50 channels and on average were within ±25 channels. To check on how much effect a ±25-channel variance on the QDC threshold had on the extracted yield, we applied QDC thresholds ±25 channels from the nominal value to the data and then extracted the yields using the same efficiency and attenuation calculations (see Sec. III.D) that were used on the data cut with the nominal QDC threshold value. It was found that a ±25-channel variance in the QDC threshold led to a ±10 to 15% variance in the double-differential yields.

III.C.3. High-Energy Wraparound Neutrons

Continuing the example from Sec. III.C.1, where it was found that neutrons from beam burst B with energies 9.3 MeV and lower wrapped around with neutrons coming from beam burst C, the same calculation can be repeated to find the energies of neutrons from beam burst A, which wrap around with neutrons from beam burst C. In this case neutrons from burst A with 2.7 MeV and lower wrap around with neutrons from burst C. Table IV contains the values of the first and second wraparound energies for each set of detectors. The first wraparound energy corresponds to neutrons from burst B, and the second wraparound energy corresponds to neutrons from burst A.

TABLE IV

First and Second Wraparound Energies for Each Set of Neutron Detectors

Detector(s) Angle (deg)	First Wraparound Energy (MeV)	Second Wraparound Energy (MeV)
10	29.6	9.3
30	29.6	9.3
45	29.6	9.3
60	23.9	7.4
90	12.6	3.7
125	11.8	3.4
160	9.3	2.7
−30	9.5	2.7
−45	9.5	2.7

Note that the region in the TDC spectrum in Fig. 2 between bursts D and C contains neutrons from burst C that have energies with the first wraparound energy and higher and neutrons from burst B that have energies between the first and second wraparound energies. Applying a QDC threshold equivalent to the first wraparound energy eliminates neutrons from all beam bursts except for burst C, while applying a QDC threshold equivalent to the second wraparound energy includes neutrons from bursts C and B. It is possible to deduce the number of counts in a specific TDC channel from burst B by eliminating the number of counts due to neutrons from burst C, referred to as the high-energy wraparound neutrons, using the following formula:

$$\mathrm{TDC}n_B(T_2) = \mathrm{TDC}n_{tot}(T_2) - \left(\mathrm{TDC}n_C(T_1) \times \frac{eff(E_C,T_2)}{eff(E_C,T_1)}\right) , \quad (2)$$

where

$\mathrm{TDC}n_B(T_2)$ = number of counts in channel n due to neutrons from burst B using a QDC threshold equivalent to the second wraparound energy

$\mathrm{TDC}n_{tot}(T_2)$ = number of counts in channel n using a QDC threshold equivalent to the second wraparound energy

$\mathrm{TDC}n_C(T_1)$ = number of counts in channel n due to neutrons from burst C using a QDC threshold equivalent to the first wraparound energy

$eff(E_C,T_2)$ = detection efficiency (Sec. III.D) for a neutron with an energy equal to the corresponding energy in channel n for a neutron from burst C using a detection threshold equal to the second wraparound energy

$eff(E_C,T_1)$ = detection efficiency at the corresponding energy in channel n for a neutron from burst C using a detection threshold equal to the first wraparound energy.

Using Eq. (2) together with QDC thresholds that correspond to the first and second wraparound energies makes it possible to extend the spectra to lower energies. For example, for the detector shown in Fig. 2, the spectrum for energies 9.5 MeV and higher is produced by applying the QDC threshold equivalent to the first wraparound energy, and the spectrum between 2.7 and 9.5 MeV is generated by applying a QDC threshold equivalent to the second wraparound energy, along with Eq. (2). The high-energy end of the spectrum produced using the second wraparound energy was checked against the low-energy end of the spectrum produced by the first wraparound energy to ensure that the two spectra matched well at the point where they meet. The spectra from all individual detectors matched well at those points. As an additional check on the method using Eq. (2), the spectra between 10 and 30 MeV at +30 and +45 deg [produced by applying Eq. (2)] were checked against the spectra between 10 and 30 MeV at −30 and −45 deg (produced by applying the QDC threshold equivalent to the first wraparound energy). In both cases, the different spectra agreed within statistical uncertainties.

III.D. Efficiency, Attenuation, and Normalization Factors

After the neutron spectra were converted from units of TDC channel number to units of energy, the spectra were corrected for neutron detection efficiency using the code developed by Cecil, Anderson, and Madey.[10] Figure 4 shows the neutron detection efficiency for detector 9 for a QDC threshold equivalent to 29.5 MeV in neutron energy. For comparison, the detection efficiency for detector 9 using a 15.5-MeV threshold is also shown.

The spectra were also corrected for the loss of neutron flux due to scattering by materials between the target and the detector. To accomplish this, a Monte Carlo code was written that included all relevant neutron elastic and inelastic scattering cross sections. Also included was all the relevant geometric information, such as detector dimensions, thicknesses of materials between the target and detector, and positions of those materials in the laboratory. The code kept track of the number of neutrons that did and did not reach the neutron detector. The

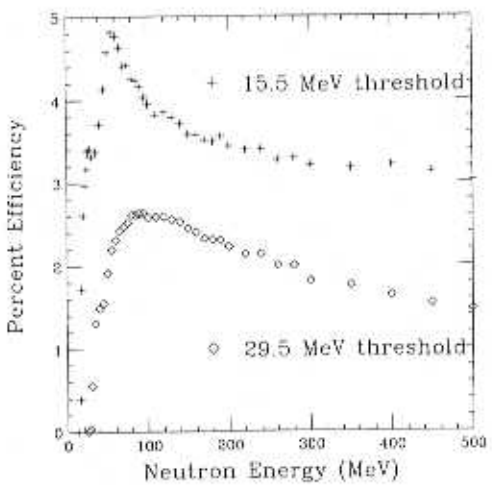

Fig. 4. Neutron detection efficiency as a function of neutron energy for detector 9, using the indicated thresholds. The efficiency was calculated using the code developed by Cecil, Anderson, and Madey.[10]

diamond-shaped symbols in Fig. 5 show the result of the calculation performed for detector 9, showing the fraction of neutrons that reach the detector as a function of neutron energy. The spectrum of actual events in detector 9 is corrected by dividing by the appropriate fraction given in Fig. 5. The results of the code used here were compared with the results of a code written by Remington.[11] The two agreed with each other to within 10%, and that value was taken as the systematic error on the flux-attenuation correction.

Unless otherwise noted, the yields reported in this paper do not include a correction for the loss of neutron flux inside the target. The amount of target material traversed by the neutron depends on both the location inside the target where the neutron was produced and on the angle at which the neutron was emitted. For example, a neutron emitted at 10 deg from He interacting in the target could go through 0.55 to 5.15 cm of Al, depending on where in the target the neutron was emitted. The nature of the neutron spectra at the point of the primary interaction in the target will depend on the location in the target because the energy of the primary ion also depends on the location within the target. Thus, to apply a correction for neutron flux attenuation through the target, the neutron production cross sections must be known for all primary interactions up to the incident primary ion energy. Not enough data exist to perform such a correction; however, if one neglects the differences in neutron spectra as a function of depth in the target, a first-order estimation of the loss of flux through the target may be obtained by stepping the primary ion through the target and performing a series of attenuation calculations for different depths of the target traversed by the emitted neutron. The X-shaped symbols in Fig. 5 show such an attenuation calculation for detector 9, including the effects of attenuation through the target.

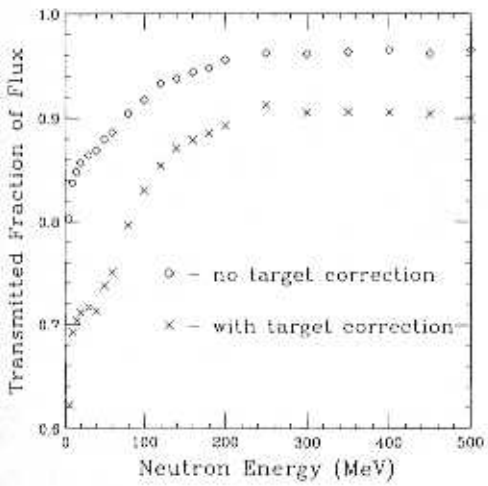

Fig. 5. Fraction of the incident neutron flux transmitted to detector 9 as a function of energy. The results of calculations are shown with and without the effect of neutron transport through the target. Unless otherwise noted, the reported spectra do not include a correction for flux lost in the target.

Neutron spectra were also corrected for computer dead time and for prescale factors. The spectra were normalized to the number of incident beam particles, which were counted by using the Al target as a Faraday cup and connecting the target to a current integrator.

The stability of the double-differential yields was checked as a function of the QDC threshold applied to the data. For example, spectra were generated for the detector at −30 deg for QDC thresholds corresponding to 10, 20, and 30 MeV. For each different QDC threshold applied to the data, a different efficiency correction must also be applied to the data. There was no observable difference within statistical uncertainties (statistical uncertainties were on the order of 5% for the spectra at −30 deg) between the three spectra corresponding to different QDC thresholds at −30 deg. The other detectors were also checked with at least two different QDC thresholds, and in all cases the spectra were the same within statistical uncertainties.

IV. EXPERIMENTAL RESULTS

The spectra reported in this paper include neutrons produced in the target by interactions of the primary ion, interactions by all secondary particles, and neutron interactions in the target. No corrections were made to the fluences caused by neutron transport through the target. All reported yields, then, pertain to the fluence as it leaves the target.

Except where noted, the uncertainties shown in the figures and tables are statistical. The systematic uncertainties mainly affect the overall scale of the spectra and include contributions from uncertainties in the efficiency calculation, flux-attenuation calculation (10%, see Sec. III.D), QDC wraparound-threshold determination (10 to 15%, see Sec. III.C), solid-angle determination, and number of incident ions.

The systematic uncertainty in the efficiency calculation was estimated by comparing the results of the calculation used here with another efficiency calculation,[12] assuming a precisely defined threshold. The two calculations disagreed by at most 10%, and that value is taken as the uncertainty in the efficiency calculation.

The systematic uncertainty in the solid angle stems mainly from the uncertainty in the location of neutron production within the stopping target and the difference in the solid angle at the front and back faces of the detector. This uncertainty is estimated by calculating the solid angles at the production point in the target nearest to the front face of the detector and at the production point farthest from the back face of the detector, and then taking half of the difference between the two values.

Because the range of the He beam is longer than the C beam, the uncertainty is greater for the He data set than it is for the C data set. The uncertainty is greatest at 160 deg, where it is 7.4% for the He + Al data and 5.0% for the C + Al data. The uncertainties for all detectors are listed in Table I.

The systematic uncertainty in the number of incident ions is primarily due to losses of delta electrons and secondary protons from the target. Using the data from the veto detectors, it was estimated that one proton escaped the target for every nine incoming He ions (a loss of 0.057 positive charge unit per incoming charge) and that one proton escaped for every 22 incoming C ions (a loss of 0.008 positive charge unit per incoming charge). The number of delta electrons knocked out of the target by escaping charged secondaries was estimated using the delta-electron-production equation of Ref. 13 and the range-energy relation of Ref. 14. We estimate between 0.1 and 2 delta electrons escape the target with each escaping charged secondary. The large uncertainty is due to the uncertainties in the calculation of low-energy delta-electron production. Using the aforementioned estimates of escaped positive and negative charges from the target, the systematic uncertainty in the number of ions is taken to be on the order of 5% for the He run and less than that for the C run.

Summing the individual contributions to the systematic uncertainty in quadrature yields an overall systematic uncertainty of 20 to 25%. As a check on the overall systematic uncertainty, the yields from detectors in the same detector bundle were compared to each other. Because the data from each detector require a separate efficiency calculation, flux-attenuation calculation, solid-angle calculation, and QDC wraparound-threshold determination, that comparison will be sensitive to the contributions to the aforementioned systematic uncertainty except for the uncertainty in the number of beam ions. The variance of the yields within the same bundle was on the order of 20%, which is in agreement with the estimated systematic uncertainty.

IV.A. Double-Differential Yield Spectra

Figure 6 shows the double-differential spectra (in units of number of neutrons per mega-electron-volt per millisteradian per incoming ion) for the ^{12}C + Al system at 10, 45, 90, and 160 deg (left plot) and at 30, 60, and 125 deg (right plot). The contribution of neutrons from the breakup of the projectile can be seen at 10 deg in the form of the broad peak that starts near 50 MeV and extends to energies above the incident energy per nucleon. The broad peak of projectile-like neutrons is in contrast to the relatively narrow peak seen in thin-target cross-section measurements (see, for example, Ref. 15) because the projectile interacts with the target at all energies up to the incident energy of 155 MeV/nucleon. At angles of 45 deg and greater, the spectra show an exponential

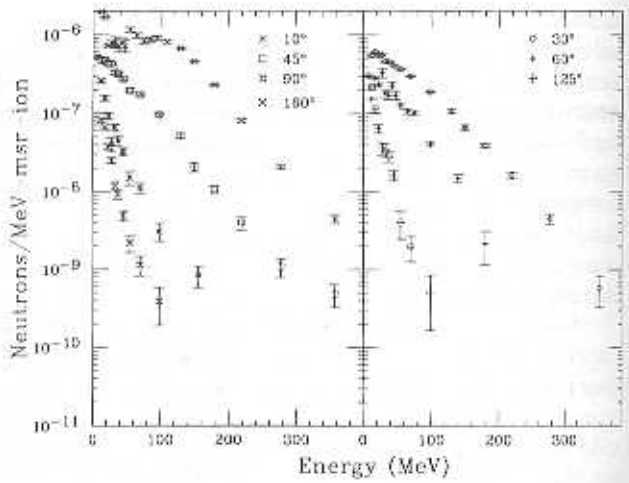

Fig. 6. Double-differential spectra for the ^{12}C + Al system at 10, 45, 90, and 160 deg and at 30, 60, and 125 deg.

fall-off with increasing energy, which is indicative of equilibrium and preequilibrium neutron emission.[16]

Figure 7 shows the double-differential spectra for the ^{4}He + Al system in the same format as in Fig. 6. The features seen in the ^{12}C + Al system can also be seen in the ^{4}He + Al system. Wider energy binning was used in the ^{4}He + Al data because the ^{4}He beam pulse was wider than the ^{12}C beam pulse (3-ns wide and 1-ns wide, respectively), which led to a larger value of the timing resolution.

As a check on overall normalization, the 45- and 90-deg ^{4}He + Al data can be compared with a similar measurement taken with 160 MeV/nucleon ^{4}He stopping in a Pb target.[17] Table V shows a comparison of yields

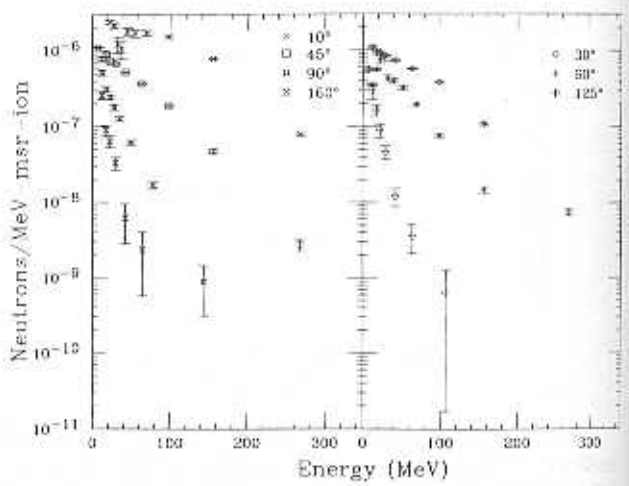

Fig. 7. Double-differential spectra for the ^{4}He + Al system at 10, 45, 90, and 160 deg, and at 30, 60, and 125 deg.

TABLE V

Comparison of 45- and 90-deg ^{4}He + Al Data with 160 MeV/Nucleon ^{4}He + Pb Data*

^{4}He + Al 155 MeV/nucleon		^{4}He + Pb 160 MeV/nucleon	
Energy (MeV)	Yield[a]	Energy (MeV)	Yield
45 deg			
17.4	886 ± 37	16.3	1080 ± 65
22.4	720 ± 36	20.9	857 ± 47
29.8	671 ± 23	27.3	655 ± 36
42.1	520 ± 15	37.1	505 ± 25
90 deg			
12.4	515 ± 46	13.2	581 ± 35
17.4	314 ± 24	17.8	381 ± 23
22.4	245 ± 17	23.8	257 ± 15
27.4	179 ± 15		
		31.8	141 ± 8
34.8	128 ± 9		
		42.3	94.4 ± 6.6
49.4	61 ± 4		
		56.2	46.7 ± 4.2
78.3	17 ± 2	81.6	19 ± 3

*From Ref. 17.

[a]In numbers per mega-electron-volt per steradian per 10^6 incoming ions.

between the two systems in numbers per mega-electron-volt per steradian per 10^6 incoming ions. The uncertainties reported in Table V are the statistical uncertainties. The main difference between the two systems is the mass of the target. However, the authors of Ref. 17 found that for 177.5 MeV/nucleon ^{4}He stopping in targets of C, water, Fe, and Pb, the total yield was independent of target mass. An analysis of the double-differential spectra from those systems shows that the yields at a particular energy and angle vary at most ±20% with target mass. A comparison between the 155 MeV/nucleon ^{4}He + Al and 160 MeV/nucleon ^{4}He + Pb data sets in Table V shows a similar variation. This indicates that the spectra reported in this paper are consistent with the only other reported stopping-target data for this ion species and energy range.

IV.B. Energy and Angular Distributions

Figure 8 shows the energy distributions for the ^{12}C + Al system (shown by the X-shaped symbol) and ^{4}He + Al system (shown by the diamond-shaped symbol). These spectra were generated by integrating the seven double-differential spectra (10, 30, 45, 60, 90, 125, and 160 deg) from 0 to 180 deg. The two systems are very similar in shape, which can be characterized as an exponential falloff with increasing energy, along with a small "hump" or "shoulder" between 50 and 200 MeV. The shoulder is likely due to the contribution from the decay of the projectile remnant. The main difference between the two systems is that the magnitude of the ^{12}C + Al spectrum is a factor of ~2 less than the ^{4}He + Al spectrum.

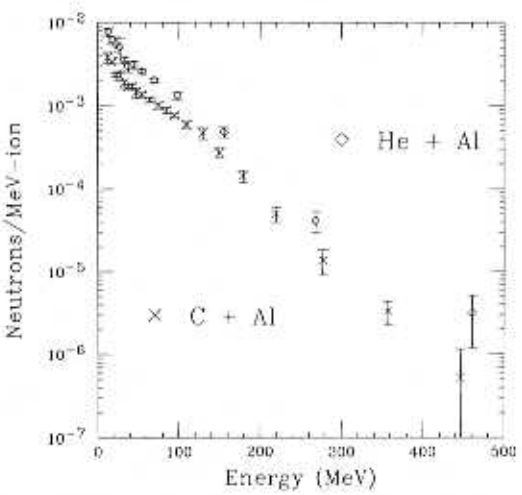

Fig. 8. Energy distributions of the neutron yield for the ^{12}C + Al and ^{4}He + Al systems.

TABLE V

Comparison of 45- and 90-deg ^{4}He + Al Data with 160 MeV/Nucleon ^{4}He + Pb Data*

^{4}He + Al 155 MeV/nucleon		^{4}He + Pb 160 MeV/nucleon	
Energy (MeV)	Yield[a]	Energy (MeV)	Yield
45 deg			
17.4	886 ± 37	16.3	1080 ± 65
22.4	720 ± 36	20.9	857 ± 47
29.8	671 ± 23	27.3	655 ± 36
42.1	520 ± 15	37.1	505 ± 25
90 deg			
12.4	515 ± 46	13.2	581 ± 35
17.4	314 ± 24	17.8	381 ± 23
22.4	245 ± 17	23.8	257 ± 15
27.4	179 ± 15		
		31.8	141 ± 8
34.8	128 ± 9		
		42.3	94.4 ± 6.6
49.4	61 ± 4		
		56.2	46.7 ± 4.2
78.3	17 ± 2	81.6	19 ± 3

*From Ref. 17.

[a]In numbers per mega-electron-volt per steradian per 10^6 incoming ions.

between the two systems in numbers per mega-electron-volt per steradian per 10^6 incoming ions. The uncertainties reported in Table V are the statistical uncertainties. The main difference between the two systems is the mass of the target. However, the authors of Ref. 17 found that for 177.5 MeV/nucleon ^{4}He stopping in targets of C, water, Fe, and Pb, the total yield was independent of target mass. An analysis of the double-differential spectra from those systems shows that the yields at a particular energy and angle vary at most ±20% with target mass. A comparison between the 155 MeV/nucleon ^{4}He + Al and 160 MeV/nucleon ^{4}He + Pb data sets in Table V shows a similar variation. This indicates that the spectra reported in this paper are consistent with the only other reported stopping-target data for this ion species and energy range.

IV.B. Energy and Angular Distributions

Figure 8 shows the energy distributions for the ^{12}C + Al system (shown by the X-shaped symbol) and ^{4}He + Al system (shown by the diamond-shaped symbol). These spectra were generated by integrating the seven double-differential spectra (10, 30, 45, 60, 90, 125, and 160 deg) from 0 to 180 deg. The two systems are very similar in shape, which can be characterized as an exponential falloff with increasing energy, along with a small "hump" or "shoulder" between 50 and 200 MeV. The shoulder is likely due to the contribution from the decay of the projectile remnant. The main difference between the two systems is that the magnitude of the ^{12}C + Al spectrum is a factor of ~2 less than the ^{4}He + Al spectrum.

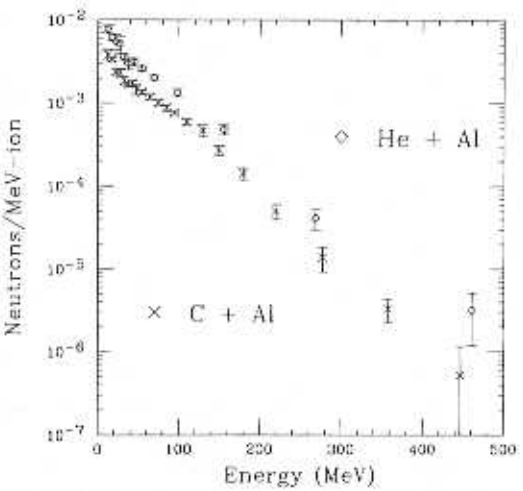

Fig. 8. Energy distributions of the neutron yield for the ^{12}C + Al and ^{4}He + Al systems.

Figure 9 shows the angular distributions from the $^{12}C + Al$ (X-shaped symbols) and the $^{4}He + Al$ (diamond-shaped symbols) systems. These distributions were obtained by integrating the double-differential spectra over energy above 10 MeV. Both spectra show the same dependence of yield on angle; the only major difference between the two is their relative magnitudes.

The solid and dashed lines in Fig. 9 show a fit to the data based on a superposition of two exponentials:

$$y = (a_1 \times e^{-(a_2 \times \theta)}) + (a_3 \cdot e^{-(a_4 \cdot \theta)}) \ , \qquad (3)$$

where a_1, a_2, a_3, and a_4 are fit parameters and y is the number of neutrons per millisteradian. Table VI shows the fit parameters for both systems, using units of degrees for θ in Eq. (3). Within uncertainties, the slope parameters a_2 and a_4 are the same for both systems.

It is also useful to compare the spectra here with proton-induced stopping target yields. We know of no experimental data for neutron production from 155-MeV protons stopping in Al; however, neutron yields from 113-MeV (Ref. 18) and 256-MeV (Refs. 19 and 20) protons stopping in Al (and a variety of other targets) have been measured, and those measurements are used for comparison with the yields reported in this paper. Table VI shows the ratios of the He- and C-induced yields to the yields from 113- and 256-MeV proton interactions for neutrons above 10 MeV at the indicated angles. Because the proton-induced data were read from compressed log-log plots presented in Refs. 18, 19, and 20, the ratios shown in Table VII are estimated to have an uncertainty on the order of 10 to 20%. One clear trend is the increase in the ratio at forward angles over that at back angles. This is indicative of the contribution from projectile fragmentation in the He and C data sets that is absent in proton interactions. It is also clear that the total yields from the 155 MeV/nucleon He and C data sets will be larger than the yields from 155-MeV protons stopping in Al; an expanded discussion of this subject may be found in Sec. IV.C.

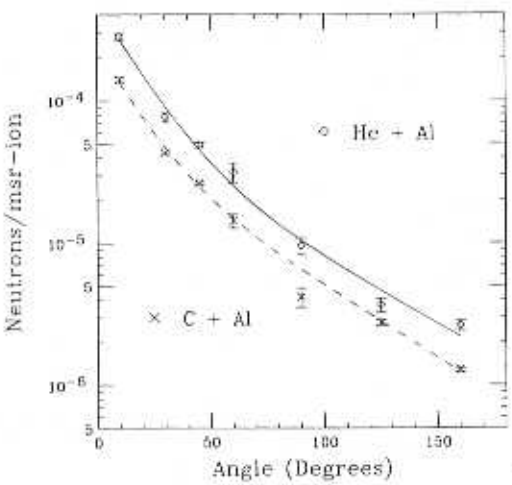

Fig. 9. Angular distributions of the neutron yield for the $^{12}C + Al$ and $^{4}He + Al$ systems. The solid and dashed lines show fits to the data, as described in the text.

TABLE VI

Fit Parameters from Eq. (3) for Both Systems*

	$^{12}C + Al$	4He+ Al
a_1	$(5.0 \pm 0.8) \times 10^{-5}$	$(6.0 \pm 0.5) \times 10^{-5}$
a_2	$(2.32 \pm 0.12) \times 10^{-2}$	$(2.1 \pm 0.3) \times 10^{-2}$
a_3	$(2.0 \pm 0.3) \times 10^{-4}$	$(4.3 \pm 0.9) \times 10^{-4}$
a_4	$(7.4 \pm 0.6) \times 10^{-2}$	$(6.6 \pm 0.8) \times 10^{-2}$

*In Eq. (3), θ is measured in degrees.

IV.C. Total Yields

Table VIII shows the total yield for each system, obtained by integrating the spectra in Fig. 8 over energy (above 10 MeV) and over angle from 0 to 180 deg. The total yields are expressed in numbers of neutrons per incident ion. Also shown in Table VIII are the estimated fractions of beam ions that undergo a nuclear interaction in the stopping target, as calculated using an energy-dependent geometric cross-section equation.[21] The fourth column in Table VIII, which shows the number of neutrons per interaction as calculated by dividing the number in the second column by the number in the third column, shows that the same number of neutrons per interaction is emitted from the $^{12}C + Al$ system as from the $^{4}He + Al$ system, within uncertainties. In both systems, the total yield is ~1 neutron above 10 MeV per interaction. The fact that the number of neutrons per interaction is the same, within uncertainties, between the two systems indicates that the total yields scale, to first order, with the expected fraction of nuclear interactions per beam ion.

The uncertainties shown for the number of neutrons per interaction do not take into account the uncertainty in the calculated total reaction cross sections. For example, using the energy-independent total reaction cross-section equation found in Ref. 22, the fraction of He + Al interactions changes from 0.34 to 0.375, and the fraction of C + Al interactions changes from 0.18 to 0.19. Using those fractions, the number of neutrons per interaction in the He + Al system is 0.93, and the number of neutrons per interaction in the C + Al system is 0.94.

As stated earlier, the yields reported in this paper do not include the effects of neutron transport through the target. Because the same target was used for both beams and because the range of He in that target is very different from the range of C through the target, correcting for neutron transport in the target may significantly

TABLE VII

Comparison of the He- and C-Induced Neutron Yields*

	$Y_{He}/Y_{113\ MeV/prot}$	$Y_{He}/Y_{256\ MeV/prot}$	$Y_C/Y_{113\ MeV/prot}$	$Y_C/Y_{256\ MeV/prot}$
$\theta_{He,C} = 10$ deg, $\theta_{prot} = 7.5$ deg	20	4	10	2
$\theta_{He,C} = 30$ deg, $\theta_{prot} = 30$ deg	9	2	5	1
$\theta_{He,C} = 60$ deg, $\theta_{prot} = 60$ deg	10	2	5	1
$\theta_{He,C} = 125$ deg, $\theta_{prot} = 120$ deg	NA[a]	1	NA	1
$\theta_{He,C} = 160$ deg, $\theta_{prot} = 150$ deg	2	1	1	0.5

*With 113- and 256-MeV proton-induced yields for neutrons with energies 10 MeV and higher at the indicated angles.
[a]Not applicable.

depend on which system is being considered. As stated in Sec. III.D, correcting for transport through the target requires knowledge of neutron-production cross sections over the entire range of interaction energies, which we do not have. However, using the simple calculation outlined in Sec. III.D to correct for the loss of flux inside the target, we estimate that the total yield for the C + Al system changes from 0.179 ± 0.005 to 0.219 ± 0.005 and that the total yield for the He + Al system changes from 0.348 ± 0.013 to 0.414 ± 0.017. The estimated number of neutrons per interaction then changes to 1.22 ± 0.03 for the C + Al system and 1.22 ± 0.05 for the He + Al system. Based on these results, correcting for neutron transport through the target changes the reported yields on the order of 20%.

The yields are also not corrected for secondary interactions in the target. Because twice as many He interactions as C interactions are estimated to occur and because the types and relative numbers of secondary particles between the two systems may be very different, it is conceivable that a correction for secondary interactions in one system will be quite different from that in the other. We present no such correction here, other than to point out that it may be different for the two systems.

The fact that the total numbers of neutrons per interaction are essentially the same for both systems despite the fact that ^{12}C has three times the number of neutrons as does ^{4}He may be due to the following:

1. The total number (20) of neutrons in the ^{12}C + Al system is close to the total number (16) of neutrons in the ^{4}He + Al system. This would suggest that the total yields are dominated by interactions that involve the breakup of the entire projectile-plus-target system. However, much of the yield at forward angles and at high neutron energies comes from the breakup of the projectile, so this reason alone cannot explain why the total yields per interaction are independent of projectile mass.

2. Nuclear structure effects, such as alpha or deuteron clustering within the nucleus, may strongly bind neutrons with other nucleons and suppress breakup channels that emit free neutrons. The breakup of the ^{12}C nucleus, which has a filled $1p_{3/2}$ subshell, may be affected at this energy by structural effects. This possibility could be tested by repeating this experiment with a projectile that has neutrons not as strongly bound, such as ^{14}N, to compare the total yields from that system to those reported in this paper.

3. The number of neutrons per interaction reported here are not the neutron multiplicities of the primary interactions because secondary interactions and neutron interactions inside the target have not been accounted for. As pointed out previously, those processes may have a significant and different effect for each system. Also, there is a non-negligible uncertainty in the calculation of the total reaction cross section for each system, which affects the calculation of the number of neutrons per interaction.

TABLE VIII

Total Yields for the Two Systems*

System	Yield	Interaction Fraction[a]	Neutrons per Interaction
^{12}C + Al	0.179 ± 0.005	0.18	0.99 ± 0.03
^{4}He + Al	0.348 ± 0.013	0.34	1.02 ± 0.04

*Expressed in number of neutrons per incoming ion.
[a]Fraction of beam particles expected to undergo a nuclear interaction in the target.

The total yield from the 155 MeV/nucleon ^{4}He + Al system is 0.35 neutrons per incoming ion for neutrons with energies >10 MeV. As noted previously, the authors of Ref. 17 found that the total yields above 10 MeV from the 177.5 MeV/nucleon ^{4}He systems were ~0.5 neutron per incoming ion, independent of target mass. They also noted that the yields from the 160 MeV/nucleon

^{4}He + Pb system were ~20% less than the yields from the 177.5 MeV/nucleon ^{4}He systems; thus, a total neutron yield of ~0.4 neutron above 10 MeV per ion is estimated for the 160 MeV/nucleon system. Because the total yield dropped from 0.5 n/ion at 177.5 MeV/nucleon to an estimated 0.4 n/ion at 160 MeV/nucleon, it is presumed that the estimated yield will drop further as the beam energy goes from 160 to 155 MeV/nucleon. Our value of 0.35 n/ion for the 155 MeV/nucleon ^{4}He + Al system is consistent with that estimate, within a systematic uncertainty of ±20%.

Figure 10 shows a plot of the total yields for both systems above a given neutron energy. The ^{4}He yields are indicated by the diamond-shaped symbols, and ^{12}C yields are indicated by the X-shaped symbols. The ratio of the yields between the two systems remains the same (2:1 for He:C) no matter which neutron-energy cutoff is used. The dependence of the total yield on neutron-energy cutoffs between 10 and 100 MeV shows a slightly different behavior from that observed in Ref. 17, which found a power-law relationship between yield and cutoff energy for cutoff energies between 1 and 50 MeV. For the data here, the best fits are obtained by using an exponential of the form

$$Y(>E) = a \times e^{-(b \times E)} ,$$

where $a = 0.20 \pm 0.03$ and $b = 0.017 \pm 0.003$ for the ^{12}C + Al system, and $a = 0.40 \pm 0.08$ and $b = 0.017 \pm 0.004$ for the ^{4}He + Al system (both fits are shown by a solid line in Fig. 10). However, if the points above 50 MeV in Fig. 10 are excluded, the remaining data are fitted reasonably well with a power-law relationship of the form

$$Y(>E) = a \times E^{-b} ,$$

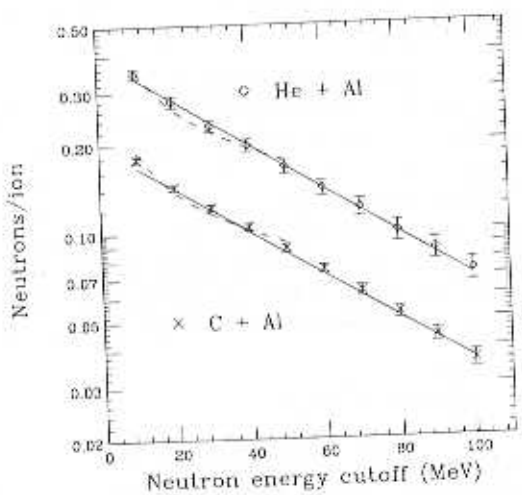

Fig. 10. Total neutron yields above a given neutron energy for ^{4}He + Al and for ^{12}C + Al. The dashed and solid lines come from fits explained in the text.

where $a = 0.52 \pm 0.05$ and $b = 0.44 \pm 0.03$ for the ^{12}C + Al system, and $a = 1.00 \pm 0.13$ and $b = 0.45 \pm 0.04$ for the ^{4}He + Al system (fits are shown by the dashed lines in Fig. 10).

Using the proton-induced data sets from Refs. 18, 19, and 20, it is estimated that the total number of neutrons above 10 MeV per incoming 113-MeV proton is ~0.04, and the total yield from 256-MeV protons is ~0.167 n/ion. Using a linear interpolation between the 113-MeV total yield and the 256-MeV total yield, it is estimated that the total yield of neutrons above 10 MeV from 155-MeV protons stopping in Al will be 0.08 n/ion. Using that number for the proton-induced total yield, we find that 155 MeV/nucleon He stopping in Al will produce 4.4 times the number of neutrons (above 10 MeV) as 155-MeV protons stopping in Al and that 155 MeV/nucleon C stopping in Al will produce 2.3 times the number of neutrons as protons stopping in Al.

V. CONCLUSIONS

Neutron yields from 155 MeV/nucleon ^{12}C and 155 MeV/nucleon ^{4}He stopping in an Al target were measured to provide data relevant to shielding issues of concern for deep-space missions, high-altitude flights, and radiation therapy using heavy-ion beams. Double-differential spectra at 10, 30, 45, 60, 90, 125, and 160 deg were measured for both systems. Comparisons of the 45- and 90-deg ^{4}He + Al spectra measured here with previously measured 160 MeV/nucleon ^{4}He + Pb spectra at the same angles show that the two measurements are consistent with each other and are consistent with neutron yield being independent of target mass. Angular and energy distributions have been extracted from the double-differential spectra, and both systems exhibit the same behavior, with the only difference being the magnitudes of each. Total neutron yields for neutron energies above 10 MeV were also extracted. Both systems have the same total yield per nuclear interaction (~1 neutron above 10 MeV per interaction) despite the fact that ^{12}C has three times the number of neutrons as does ^{4}He. This result may be an indication that nuclear structure effects within these two ions favor other breakup channels over neutron decay channels for neutron energies above 10 MeV. Because the effects of secondary interactions and neutron interactions in the target were not included, it may also point to the significance of those two processes for the total neutron yields measured for this paper.

ACKNOWLEDGMENTS

The authors wish to thank the staff of the NSCL for their help and support during all stages of the experiment. We also

thank D. Green and X. Leon for their assistance with the data analysis.

This work was supported in part by the National Science Foundation under grants PHY92-14992 and INT91-13997, by the Hungarian government under grant OTKA T16059, and by NASA under grants L14230C and NSG-1-1527 and contract H-29456D.

REFERENCES

1. L. C. SIMONSEN and J. E. NEALY, "Radiation Protection for Human Missions to the Moon and Mars," Technical Paper 3079, National Aeronautics and Space Administration (1991).

2. "Radiation Exposure and High-Altitude Flight," Commentary No. 12, National Council on Radiation Protection and Measurements (1995).

3. J. A. SIMPSON, "Introduction to the Galactic Cosmic Radiation," *Composition and Origin of Cosmic Rays*, p. 1, Reidel Publishing, Dordrecht, Netherlands (1983).

4. L. C. SIMONSEN, J. E. NEALY, L. W. TOWNSEND, and J. W. WILSON, "Radiation Exposure for Manned Mars Surface Missions," Technical Paper 2979, National Aeronautics and Space Administration (1990).

5. F. A. CUCINOTTA, "Calculations of Cosmic-Ray Helium Transport in Shielding Materials," Technical Paper 3354, National Aeronautics and Space Administration (1993).

6. T. FOELSCHE, R. B. MENDELL, J. W. WILSON, and R. R. ADAMS, "Measured and Calculated Neutron Spectra and Dose Equivalent Rates at High Altitudes; Relevance to SST Operations and Space Research," TN D-1383, National Aeronautics and Space Administration (1974).

7. J. W. WILSON, J. E. NEALY, F. A. CUCINOTTA, J. SHINN, F. HAJNAL, M. REGINATTO, and P. GOLDHAGEN, "Radiation Safety Aspects of Commercial High-Speed Flight Transportation," Technical Paper 3524, National Aeronautics and Space Administration (1995).

8. J. H. HELTSLEY, L. BRANDON, A. GALONSKY, L. HEILBRONN, B. A. REMINGTON, S. LANGER, A. VANDERMOLEN, and J. YURKON, "Particle Identification via Pulse-Shape Discrimination with a Charge-Integrating ADC," *Nucl. Instrum. Methods A*, **263**, 441 (1988).

9. J. F. JANNI, "Proton Range-Energy Tables," *At. Data Nucl. Data Tables*, **27**, 2–5 (1982).

10. R. A. CECIL, B. D. ANDERSON, and R. MADEY, "Improved Predictions of Neutron Efficiency for Hydrocarbon Scintillators from 1 MeV to about 300 MeV," *Nucl. Instrum. Methods*, **161**, 439 (1979).

11. B. A. REMINGTON, PhD Thesis, Michigan State University (1986).

12. R. J. KURZ, Internal Report No. URCL-11339, University of California Radiation Laboratory (1964).

13. PARTICLE DATA GROUP, "Review of Particle Properties," *Phys. Rev. D*, **45**, Sec. III, 14 (1992).

14. L. KATZ and A. S. PENFOLD, "Range-Energy Relations for Electrons and the Determination of Beta-Ray End-Point Energies by Absorption," *Rev. Mod. Phys.*, **24**, 28 (1952).

15. A. R. BALDWIN, R. MADEY, W.-M. ZHANG, B. D. ANDERSON, D. KEANE, J. VARGA, J. W. WATSON, G. D. WESTFALL, K. FRANKEL, and C. GALE, "Inclusive Neutron Cross Sections from Ne-Pb Collisions at 790 MeV/Nucleon," *Phys. Rev. C*, **46**, 258 (1992).

16. T. NAKAMURA, "Neutron Energy Spectra Produced from Thick Targets by Light-Mass Heavy Ions," *Nucl. Instrum. Methods A*, **240**, 207 (1985).

17. R. A. CECIL, B. D. ANDERSON, A. R. BALDWIN, R. MADEY, A. GALONSKY, P. MILLER, L. YOUNG, and F. M. WATERMAN, "Neutron Angular and Energy Distributions from 710-MeV Alphas Stopping in Water, Carbon, Steel, and Lead, and 640-MeV Alphas Stopping in Lead," *Phys. Rev. C*, **21**, 2471 (1980).

18. M. M. MEIER, D. A. CLARK, C. A. GOULDING, J. B. McCLELLAND, G. L. MORGAN, and C. E. MOSS, "Differential Neutron Production Cross Sections and Neutron Yields from Stopping-Length Targets for 113-MeV Protons," *Nucl. Sci. Eng.*, **102**, 310 (1989).

19. M. M. MEIER, C. A. GOULDING, G. L. MORGAN, and J. L. ULLMANN, "Neutron Yields from Stopping- and Near-Stopping-Length Targets for 256-MeV Protons," *Nucl. Sci. Eng.*, **104**, 339 (1990).

20. M. M. MEIER, W. B. AMIAN, C. A. GOULDING, G. L. MORGAN, and C. E. MOSS, "Neutron Yields from Stopping-Length Targets for 256-MeV Protons," *Nucl. Sci. Eng.*, **110**, 299 (1992).

21. R. K. TRIPATHI, F. A. CUCINOTTA, and J. W. WILSON, "Accurate Universal Parameterization of Absorption Cross Sections," *Nucl. Instrum. Methods B*, **117**, 347 (1996).

22. R. MADEY, B. D. ANDERSON, R. A. CECIL, P. C. TANDY, and W. SCHIMMERLING, "Total Inclusive Neutron Cross Sections and Multiplicities in Nucleus-Nucleus Collisions at Intermediate Energies," *Phys. Rev. C*, **28**, 706 (1983).